ADVANCED FUNCTIONAL MATERIALS
www.afm-journal.de

Zero-Power Shape Retention in Soft Pneumatic Actuators with Extensional and Bending Multistability

*Shakurur Rahman, Lei Wu, Asma El Elmi, and Damiano Pasini**

Power-free shape retention enables soft pneumatic robots to reduce energy cost and avoid unexpected collapse due to burst or puncture. Existing strategies for pneumatic actuation cannot attain motion locking for trajectories combining extension and bending, one of the most common modes of operation. Here, a design paradigm is introduced for soft pneumatic actuators to enable zero-power locking for shape retention in both extension and bending. The underpinning mechanism is the integration of a pneumatic transmitter and a multistable guider, which are programmed to interact for balanced load transfer, flexural and extension steering, and progressive snapping leading to state locking. Through theory, simulations, and experiments on proof-of-concept actuators, the existence of four distinct regimes of deformation is unveiled, where the constituents first interact during inflation to attain locking in extension and bending, and then cooperate under vacuum to enable fully reversible functionality. Finally, the design paradigm is demonstrated to realize a soft robotic arm capable to lock at desired curvature states at zero-power, and a gripper that safely operates with puncture resistance to grasp and hold objects of various shapes and consistency. The study promises further development for zero-power soft robots endowed with multiple deformation modes, sequential deployment, and tunable multistability.

1. Introduction

Soft robots have gained traction over the last decade due to their intrinsic capacity to safely interact with human and delicate objects, as well as to nimbly adapt to a harsh changing environment.[1–10] The softness and high deformability of their base material as well as their architecture enable them to morph their body, easily reconfigure and deform around object profiles, making them suitable for applications that include wearable assistive devices,[11–13] search and rescue robots[14–16] and compliant grippers.[17–21] Compliant robotic systems are often designed to operate under a pneumatic pressure, where actuation is dispensed through a pneumatic network of fluidic conduits that is laid out to guide their deformation and reconfigure in desired target shapes.

One key characteristic of existing pneumatic soft robots pertains to their unceasing reliance on pressure supply to operate. Upon removal of the pressure source, they all promptly return to their initial state, hence being unable to hold any intermediate state configuration without a continuous pressure supply.[22–24] While this response enables morphing reversibility, it has a twofold undesired outcome. First, to maintain a given shape posture, a nonstop supply of pressure is needed, a requirement that attests an inefficient use of energy resource. Second, if a puncture or burst occurs, the soft robot halts abruptly its operation, potentially leading to harmful consequences. To bypass these limitations, hence improving the use of energy resource and, even more critically, ensuring the safe operation of a soft robot, it is highly desirable to design soft robots that can lock-in a desired target shape without relying on the constant provision of pressure or another means of actuation.

Shape lockability in soft robots has been explored in the literature through non-pneumatic and pneumatic means of actuation. The former can achieve locking in both extension and bending but requires a complex set of operational requirements and accurate manipulation of the actuation field. The latter are successful in bending only and thus unable to provide extensional locking during the axial drive of a soft robot.

Non-pneumatic actuation[25–27] typically involves the use of one or more smart materials, capable of deforming in response to an actuation input, such as electricity,[28–37] a magnetic field[38–40] and light.[41,42] A classical concept consists of two layers, one stimuli-responsive and the other strain-limiting; due to either chemical changes[42] or phase transitions[36,41] within each layer, bending deformation is attained with locking in given states. To achieve locking in both bending and extension, concepts that rely on elastic bistable elements have been proposed where instability is induced by an external field. Some leverage either an electric field[33–35] or a magnetic field[38] in carbon fiber reinforced

S. Rahman, L. Wu, A. El Elmi, D. Pasini
Department of Mechanical Engineering
McGill University
Montreal, Quebec H3A 0C3, Canada
E-mail: damiano.pasini@mcgill.ca

The ORCID identification number(s) for the author(s) of this article can be found under https://doi.org/10.1002/adfm.202304151

DOI: 10.1002/adfm.202304151

polymer (CFRP) laminates to achieve shape lockability in zero-power grippers; others resort to pre-buckled elastic beams actuated using joule heating of two twisted-and-coiled actuators (TCAs) to switch between two stable bending states.[37] A similar strategy has been applied in pre-buckled elastic sheets, connected with two dielectric elastomers to reversibly shift between stable states in response to a voltage input.[29,31] Orthogonally pre-stressed dielectric elastomers attached to a strain limiting layer have also resulted in a bistable tape-spring actuator with an initial rectangular state and a deformed coiled state.[30] For lockability in extension, building blocks using the kresling origami pattern have been proposed for use under the application of either a magnetic field[39,40] or electric motors.[43–45] In the latter, both extension and bending lockability have been achieved for a crawling robot. Although strategies of non-pneumatic actuation have advantages, such as remote and local actuation, their primary drawbacks include the need for fairly complex loading patterns to function, the precise control of the actuation field, and a set of high voltage electronics that can overheat, all circumventable through pneumatic strategies especially those capable of operating via a single input channel.

Pneumatic actuation that leverages the properties of metamaterials for target shape retention is much less explored in the literature and is primarily limited to bending lockability only. Bistability in CFRP[46–48] and other pre-stressed elements such as elastic steel strip,[49] elastomeric layers,[50] and linear springs[51] have been used for zero-power bending deformation driven by pneumatic actuation. However, to attain reversibility, they generally require two or more pneumatic input channels or an additional actuation method. Reversibility using single input channel has been demonstrated using soft sheets with an array of bistable domes that can invert and produce bending deformation,[52] and an origami structure that can deploy a bistable arc and tent.[53] Other examples using single input channel include monostable pre-curved elastomeric layers,[50,54] which can grasp objects in their initial stable state without continuous power input, but entails a slower response time. All these concepts can provide a bending deformation mode, but none of them can achieve lockability in linear extension, a deformation mode that is key in soft robotics to drive axial motion,[55–57] and can minimize energy consumption. Furthermore, combining both extensional and bending lockability within a single pneumatic soft robot is currently unexplored; this functionality is a challenge even for non-pneumatic actuators, where the only demonstration delivering both extensional and bending lockability[43] requires the application of two motors cooperating in a complex manner as opposed to a simple on/off actuation.

In this work, we present a soft pneumatic actuator that can attain shape locking in extension and bending without resorting to any additional energy resource and can operate with one single input channel. The concept integrates a pneumatic transmitter with a multistable guider, whose interplay is instrumental to attain unprecedented functionalities: i) electronics-free deployment using a simple hand pump and locking into target shape upon pressure source removal, and ii) reversible deformation and full retraction to its initial actuator state under pneumatic vacuum. We first introduce the concept integrating the transmitter, here realized via an airtight chamber periodically stiffened with concentric rings, and the snapping guider directing and locking the actuator into either extension or bending. The interplay between them is investigated through a combination of numerical and theoretical models as well as experiments with results unveiling how their cooperation enables distinct regimes of functionality during a full pneumatic cycle. Finally, we showcase the application of our concept to design a soft pneumatic arm and a gripper; the former leveraging the deformation and locking in both extension and bending to attain programmable curvature in the deployed stable state, and the latter utilizing zero-power locking in bending to grasp delicate objects, thereby boosting energy efficiency.

2. Inflatable Actuator Leveraging the Interaction between a Pneumatic Transmitter and a Multistable Guider

To achieve the functionality of extensional and flexural morphing with locking under pressure supply, we present an integrated multistable inflatable actuator (**Figure 1**a top) that incorporates an inner pneumatic transmitter, *T*, and a multistable guider, *G*. The former acts as a pneumatic chamber but it consists not only of a wrinkled polyethylene cylindrical membrane but also wooden ring stiffeners periodically attached to its surface along its length (Figure 1a, bottom). The latter acts as the external frame and is made of a thermoplastic polyurethane (TPU) hexagonal cylinder comprising stacked rings with periodically arranged and geometrically tailored snapping units. While *T* and *G* are connected only at their ends via wooden plates, it is through their interaction that we can attain flexural and extensional lockability, a functionality unachievable by employing either of the two alone as explained below.

Figure 1b illustrates the role of the actuator constituents in a qualitative plot, strain energy versus displacement of the end plate. To understand the interaction between *T* (continuous line) and *G* (dashed line), we depict their contribution individually during a full pneumatic cycle of inflation $+\Delta p$ (blue), pressure release $-\Delta p$ (green), vacuum $-\Delta p$ (red) and pressure release $+\Delta p$ (green curve). Both the transmitter and the guider govern the storage and release of energy of the multistable actuator that depends on their energy states $[E_t, E_g]$. Upon inflation, *T* unravels the polyethylene wrinkles ($\overrightarrow{AB}$ in Figure 1b) and extends along its longitudinal axis as opposed to radially due to the inextensibility of its base material. As soon as *T* extends to engage the end plates, an axial force is transferred first to the end plates and then to *G*, which undergoes a tensile force that initiates a sequence of snap-through instabilities (*G, F, D* in Figure 1b), where each valley corresponds to the deployed stable state of a snapping ring. At full inflation (*B* in Figure 1b), all rings are fully deployed. Upon pressure removal, *G* reaches a stable state (*D* in Figure 1b) with energy E_G^D, whereas the wrinkles in *T* undergo stress relaxation (C in Figure 1b), with negligible storage of energy ($E_T^C \approx 0$); this occurs because during inflation, *T* deforms via unraveling of wrinkles as opposed to polyethylene stretching.[14] Because at zero pressure, *T* does not store any energy of deformation and does not hinder the guider bistability, the actuator can lock-in its deployed shape and retain it without any continuous pressure supply.

After pressure release (green), the pneumatic cycle continues under vacuum (red). From the deployed states of *T* and

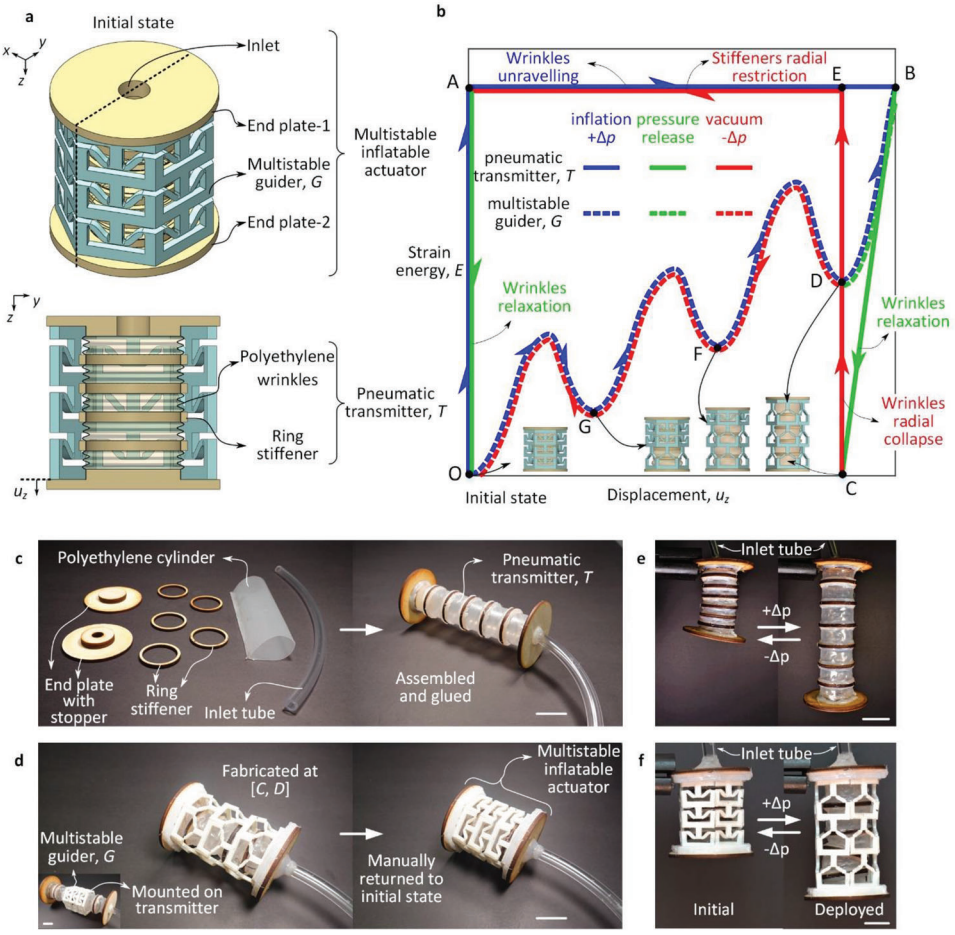

Figure 1. Multistable inflatable actuator for zero-power shape retention and reversible deformation. a) 3D model (top) with cross-section about mid-plane (bottom), showing multistable guider *G*, pneumatic transmitter *T* with wrinkled polyethylene cylinder, wooden ring stiffeners, and end plates. b) Qualitative plot (strain energy against displacement) unveiling the physical mechanism of interaction between *T* and *G*, as the actuator undergoes a pneumatic cycle of inflation $+\Delta p$, pressure release $-\Delta p$, vacuum $-\Delta p$ and pressure release $+\Delta p$. Stable deployed state [*C*, *D*] is retained without continuous pressure supply. Pneumatic vacuum enables the actuator to return to its initial stable state *O*. c) Individual components of *T* are shown prior to and post-assembly operation. d) Inflatable actuator fabricated at deployed energy state [*C*, *D*] by first mounting *G* on *T*, manually deforming them to their deployed state followed by bonding of end plates. e) Axial expansion and contraction of standalone pneumatic transmitter upon application of $+\Delta p$ and $-\Delta p$. f) Reversible transition between condensed state and locked state, both retained without pressure supply, upon pneumatic inflation and vacuum. Scale bars = 2 cm.

G [respectively *C*, *D* in Figure 1b], the polyethylene wrinkles of *T* start to collapse radially ($\overrightarrow{CE}$) but its wooden ring stiffeners impede the radial collapse and guide the deformation of *T* into axial contraction, thereby playing a key role in ensuring the reversibility of our multistable inflatable actuator. Without ring stiffeners, the curve ($\overrightarrow{EA}$) of *T* would be lost, and the transmitter will simply collapse radially under pneumatic vacuum. Hence, the role of ring stiffeners is essential for *T* to exert the compressive force on *G* under pneumatic vacuum. This enables the actuator to snap-through to its initial, closed state [*O*], hence ensuring full reversibility with no need for any mechanical force. Upon removal of the vacuum pressure, the polyethylene wrinkles relax and regain the initial energy state [*O*].

Realizing the integration of *T* and *G* into our multistable actuator requires a distinct sequence of operations, first the fabrication with straightforward steps and then the assembly requiring a specific process which we emphasize here. For *T* (Figure 1c), end plates, stoppers, and ring stiffeners are laser cut from a wooden plate and then affixed with an epoxy glue (Adhaero 5 Min Epoxy), while a polyethylene sheet is rolled into a cylinder, sealed with an impulse sealer, and glued to the wooden parts along with an inlet tube. For *G*, we 3D print each side of the hexagonal cylinder using TPU (ANYCUBIC Vyper), and bond them together at given location (see Section S1.2, Supporting Information). Then, the assembly of *T* and *G* into our multistable inflatable actuator follows a specific sequence of steps. The guider is first mounted on the transmitter at the initial energy state [*O*], and then manually deployed via a mechanical pull to the energy state [*D*]. Mechanical compression is applied to the end plates of *T* until it is in contact with the guider ends, wherein *T* reaches the energy state [*C*]. The end plates and the guider ends are then glued to complete the fabrication of the multistable inflatable actuator at the energy state [*C*, *D*] (Figure 1d), which is retained at zero-pressure. This ensures that the deployed state of the actuator is also retained

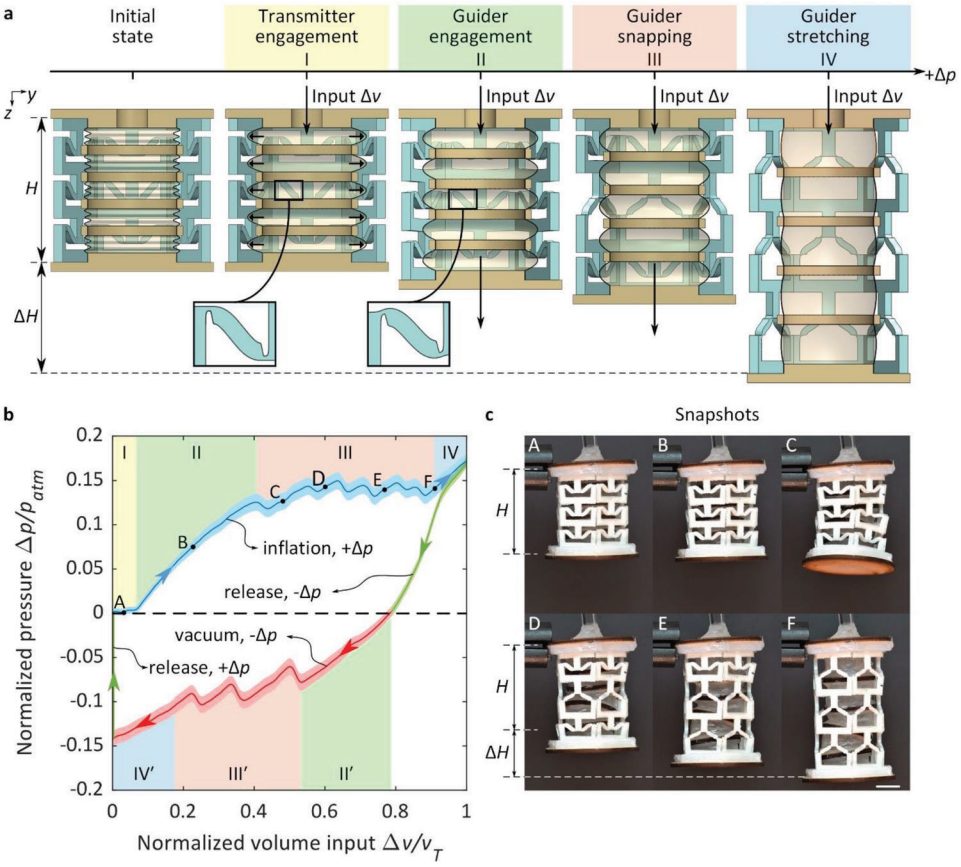

Figure 2. Interaction between multistable guider and pneumatic transmitter under pneumatic loading. a) Schematics of inflatable actuator cross-section in the four regimes of interaction: *transmitter engagement*, *guider engagement*, *guider snapping*, and *guider stretching*. b) Experimental pressure-volume response of the actuator consisting of three multistable rings undergoing a pneumatic loading loop of inflation $+\Delta p$ (blue), pressure release $-\Delta p$ (green), vacuum $-\Delta p$ (red), and pressure release $+\Delta p$ (green). Regimes of interaction highlighted with pertinent color. Uncertainty domain of experimental response indicates the dispersion of five repetitions using one sample. Pressure normalized by atmospheric pressure p_{atm}, and volume by total volume input v_T. c) Representative snapshots of multistable actuator under inflation, undergoing intermediate steps of deformation until its fully deployed stable state. Scale bar = 2 cm.

at zero-pressure when it is inflated to [*C*, *D*] during operation. A final mechanical compression enables the return to the closed initial stable state [*O*], ready for operation. Figure 1e shows the standalone response of the pneumatic transmitter under inflation (axial extension) and vacuum (contraction), and Figure 1f shows the actuator in its two stable states enabling reversible switching through inflation and vacuum.

3. Regimes of Deformation during a Full Pneumatic Cycle

To quantitatively characterize the interplay between *T* and *G*, we track the pressure-volume response of the inflatable actuator during a full pneumatic cycle of inflation and vacuum. From the experimental response, we identify four regimes of interaction (**Figure 2**a), each describing the emergence of a distinctive mechanism of deformation: *transmitter engagement*, *guider engagement*, *guider snapping*, and *guider stretching* from its initial state at rest. These are regimes depicted in the experimental pressure-volume response (Figure 2b) and snapshots of the actuator prototype at representative instances (Figure 2c).

In regime I (Figure 2a), only the wrinkles of the pneumatic transmitter are active. Under volume increase, they undergo radial outward deformation, as the axial stiffness of the snapping layer restricts deformation along the *z*–axis. This process is accompanied by a negligible increase in pressure with respect to the volume input (Figure 2b). Upon further increase in input volume, *T* starts to unravel axially due to the inextensibility of polyethylene, until it engages *G*. Here (regime II), the wooden end plates of *T* pull *G* providing a monotonic increase in pressure with respect to volume (Figure 2b). As soon as the tension exerted by *T* on *G* overcomes the energy barrier of one of its outer rings, the first snap-through event occurs (regime III), and subsequent snapping, each denoted by negative incremental stiffness, occurs in sequence until all the rings have snapped through. During axial deployment, the actuator undergoes intermediate snapping states with tilted deformation, as shown in the middle ring of snapshot C (Figure 2c) and corresponding to the first drop in pressure in Figure 2b. This phenomenon is caused by manufacturing defects; it is manifest in a given ring as asynchronous snapping of its unit cells, and characterizes the six drops in pressure,

two per ring, that can be observed in regime III of Figure 2b. This regime is entirely driven by the snap-through instability of the guider rings as they transition to their extended stable state, a process that creates space to the polyethylene wrinkles for further axial unraveling along the z–axis with subsequent volume increase. Once all rings have snapped, any further increase in input volume can only cause guider stretching, (regime IV).

The pneumatic cycle continues with pressure release (green curve in Figure 2b), followed by vacuum (red curve). The incremental application of negative volume triggers a reverse sequence of deformation (see Section S2.1, Supporting Information), with the exception of regime I, now absent due to the full extension of the transmitter wrinkles at the onset of vacuum. During vacuum, the polyethylene component of the transmitter directly undergoes axial contraction, thereby engaging the guider and generating compression (regime II′). With further negative pressure, each guider ring sequentially snaps-through to its condensed state (regime III′), until the whole guider is fully condensed and no further snapping is possible. At this stage (regime IV′), a decrease in volume can only further compress the guider. The pneumatic cycle completes with a final pressure release (green curve), wherein the internal pressure returns to zero at $\Delta v = 0$, where the inflatable actuator stabilizes due to the removal of the air volume supply.

By comparing the actuator response during inflation and vacuum, we observe a difference in the energy barriers offered by the snapping rings. During inflation, the energy barrier is much higher than during vacuum. This is because the vacuum pressure makes the unit cells within one ring to snap concurrently, that is, synchronous snapping, which results in one pressure drop per ring (at $\Delta p/p_{atm} \approx -0.1$) as opposed to two observed (at $\Delta p/p_{atm} \approx 0.15$) during inflation.

4. Energetics and Kinematics of the Multistable Guider in Extension and Bending

The previous analysis has unveiled the interplay taking place during the pneumatic cycle (inflation-release-vacuum-release) between the transmitter and the multistable guider undergoing multiple snapping events. Whether snapping can occur with monostability or bistability strongly depends on the constituent geometric parameters. In this section, we search for the defining range of geometric parameters enabling to program deployed states that lock in either extension or bending without any pressure supply. We do so by first analyzing a single unit cell and then its tessellation in a ring.

We define the unit cell geometry with an overall horizontal span l, and vertical height h, and curved beams of thickness t_b, amplitude a, and hinges of thickness t_h on its point of connections with the vertical beams (**Figure 3**a) (additional details Section S1.1, Supporting Information). Dimensionless parameters governing the lockability are here specified as the amplitude-to-horizontal span ratio a/l and the beam-to-hinge thickness ratio t_b/t_h. As the unit cell is tessellated to form a guider ring, we introduce an additional geometric variable $\nabla(a/l)$, which is the gradient governing the reduction in amplitude (a/l) as we trace the polygon of the snapping ring. This gradient $\nabla(a/l)$ is defined for an even-sided polygonal ring of m sides as:

$$\nabla\,(\mathrm{a/l}) = \; 1 - \frac{(a/l)_{P(i+1)}}{(a/l)_{Pi}}, i = 1, 2, \cdots, m/2 \tag{1}$$

where $(a/l)_{Pi}$ is the amplitude ratio of the unit cell positioned at the i^{th} side of the polygon and $(a/l)_{P(i+1)}$ at the $(i{+}1)^{th}$ side as i changes from side 1 to $m/2$ (Figure 3a).

For $\nabla(a/l) = 0$, all unit cells periodically tessellate the ring with a given amplitude-to-horizontal span ratio, hence enabling extensional snapping only. This is shown in red in a plot (Figure 3b) correlating discrete values of a/l with the unit cell position P_i. For $\nabla(a/l) > 0$, the tessellation is no longer periodic, and a gradient can be assigned to the amplitude ratio variation within the tessellated ring, hence resulting in a distinct level of bending represented by a shading of blue. For given $\nabla(a/l)$ and $(a/l)_{P1}$, the highest amplitude for a unit cell positioned on the first side of the ring (*P1* in Figure 3a), Equation (1) allows to calculate the amplitude ratio a/l for the other unit cells up to the $(m/2{+}1)^{th}$ side, with the smallest amplitude unit cell in an even-sided polygonal ring. For a hexagonal ring with $m = 6$, the smallest amplitude unit cell occupies the fourth side of the ring (*P4* in Figure 3a). The unit cells occupying the intermediate sides, that is, second and third sides can then be mirrored about the midplane to complete the assignment of unit cells within the snapping ring. As $\nabla(a/l)$ increases, a larger deviation appears between $(a/l)_{P1}$ and $(a/l)_{P4}$, which in turn imparts a bending angle in the deployed state (Figure 3b), as further discussed in Section 4.2. We emphasize that existing beam-based cylindrical metamaterials are unable to bend, a functional response that we attain in this work by introducing only one extra design variable, that is, the amplitude gradient $\nabla(a/l)$.

4.1. Programming Extension Lockability

To investigate bistable snapping in extension, we first examine rings with identical unit cells. Due to periodicity, we focus on one unit cell and assess its bistability from the strain energy curve (inset in Figure 3c), through the ratio of E_{max} (peak energy value) over E_{min} (local energy minimum). We explore the role of the geometric parameters a/l and t_b/t_h on bistability and attainable extension in the deployed state via finite element (FE) simulations (see Section S1.4, Supporting Information) and generate the corresponding phase maps for E_{max}/E_{min} (Figure 3c) and axial strain ϵ_z specifying the position of the second stable state; ϵ_z is defined as $\Delta h/h$ where Δh is the difference between the vertical height of the unit cell in its second stable state h' and its initial height h (Figure 3d). The phase maps show that for smaller a/l and t_b/t_h, snapping is mainly monostable; hence, a lower bound of 0.1 and 1 is enforced respectively on a/l and t_b/t_h, whereas for an increase of a/l and t_b/t_h, both E_{max}/E_{min} and ϵ_z raise, hence a representative upper bound of 0.4 and 4 is assigned respectively. Between these bounds, a threshold boundary (red) emerges discriminating monostability from bistability. In the case of E_{max}/E_{min}, a larger value indicates that the unit cell has a larger energy barrier, hence being more robust to perturbations and requiring a larger compressive force to initiate the snap-through to its initial

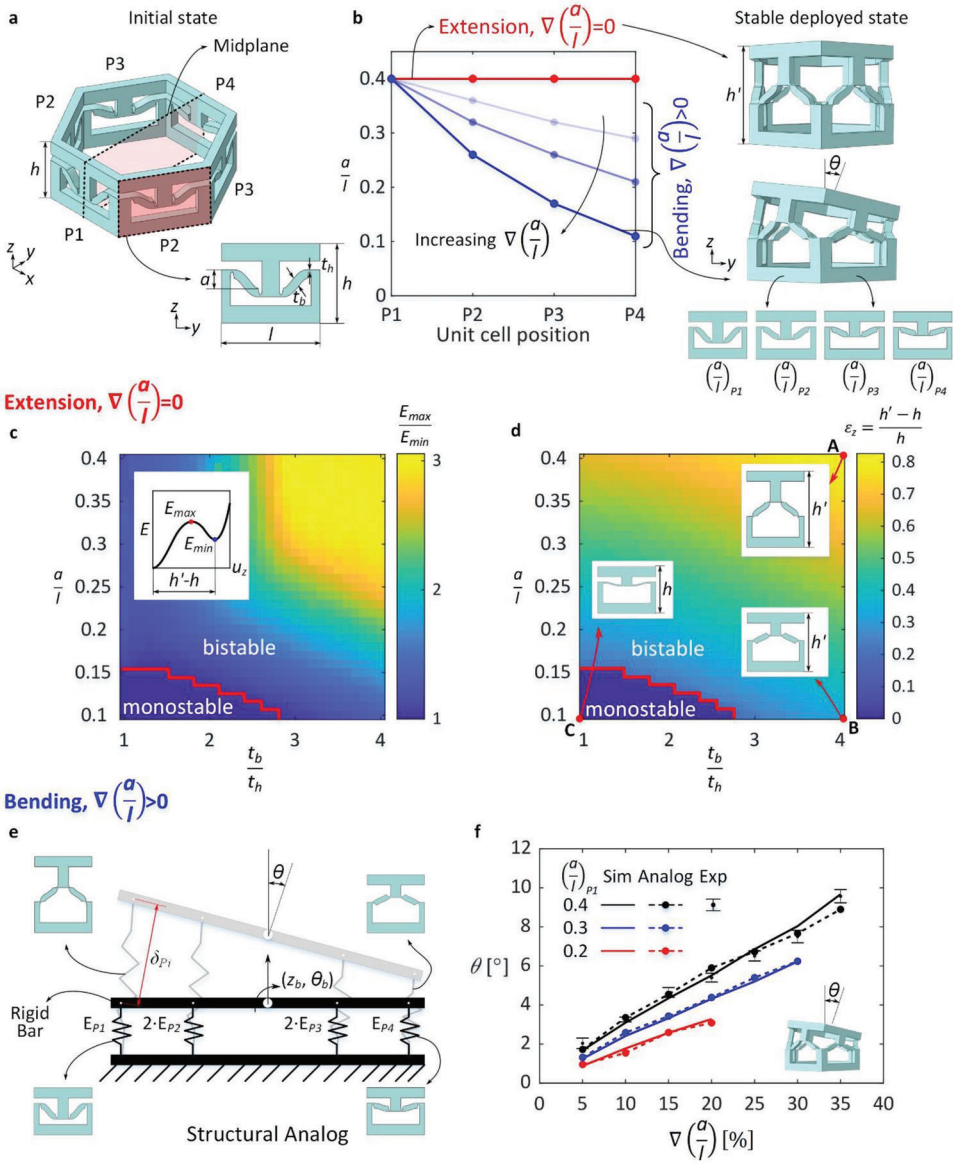

Figure 3. Energetics and kinematics of multistable guider in extension and bending. a) Guider ring with unit cell positions marked from *P1* to *P4*. Unit cells defined by horizontal span *l*, vertical height *h*, curved beams of thickness t_b, amplitude *a*, and hinges of thickness t_h. b) Variation of amplitude-to-horizontal span ratio *a*/*l* across unit cells in a ring as a function of gradient $\nabla(a/l)$. For $\nabla(a/l) = 0$, the ring extends to its second stable state with height h'. For $\nabla(a/l) > 0$, a gradient in amplitude for unit cells in the ring generates bending deformation. c) Phase diagram depicting E_{max} (peak strain energy) over E_{min} (local strain energy minimum) illustrating the role *a*/*l* and t_b/t_h in governing bistability. $E_{max}/E_{min} > 1$ indicates bistable unit cell. d) Phase diagram showing the effect of *a*/*l* and t_b/t_h on ϵ_z at the second state, where ϵ_z is given by $\Delta h/h$ with $\Delta h = h' - h$. Bistable unit cells A and B retain their deformed state, as opposed to monostable unit cells, for example, C. e) Structural analog for bending snapping ring, with non-linear springs denoting each unit cells. f) Bending angle θ of guider ring in its second state plotted as function of $\nabla(a/l)$. Results obtained via FE simulation, analog model, and experiment on proof-of-concept prototypes with $(a/l)_{P1} = 0.4$, where measurements were taken five times for each data point.

position. Points *A* and *B* in Figure 3d are representative bistable units retaining their deployed state upon load removal but each with its own axial strain attained in the second state. In contrast, monostable unit cells return to their initial state following the removal of the applied load, for example, unit cell C, hence showing no axial strain (Figure 3d).

The phase maps in Figure 3c and Figure 3d pertain to a single extensional ring. To form a multistable guider with stacking ring, for example, in Figure 1a, we tessellate the snapping ring *n* times axially, and calculate the total axial strain $\epsilon_z^{\text{total}}$ as the summation of the strain ϵ_z^j of each ring:

$$\epsilon_z^{\text{total}}\left((a/l)^j,\ \left(t_b/t_h\right)^j, n\right) = \sum_{j=1}^{n} \epsilon_z^i\left((a/l)^j,\ \left(t_b/t_h\right)^j\right) \quad (2)$$

where, $(a/l)^j$ and $(t_b/t_h)^j$ are the amplitude-to-horizontal span ratio and beam-to-hinge thickness ratio of unit cells in the extension ring *j*.

4.2. Programming Bending Lockability

To investigate locking in flexural mode, we resort to a combination of theory, simulations, and experiments, all employed to gain a deeper level of insights into the parameters that control the actuator response. We first develop a structural analog of a tilted ring (Figure 3e) that allows the prediction of bending at the ring level, and then assess and validate the tilting capacity via FE simulations and experiments (Figure 3f).

The structural analog of a snapping ring models each unit cell *Pi* with a representative nonlinear spring *Pi* characterized by an energy response $E_{Pi}(\delta_{Pi})$ obtained previously via finite element simulations of each unit cell *Pi*. The total energy of the analog model E_{total} for an even-sided polygon of m sides can be expressed as:

$$E_{\text{total}}\left(z_b, \theta_b\right) = E_{P1}\left(\delta_{P1}\right) + E_{P(m/2+1)}\left(\delta_{P(m/2+1)}\right) + 2 \cdot \sum_{i=2}^{(m/2)} E_{Pi}\left(\delta_{Pi}\right) \quad (3)$$

where, z_b is the vertical displacement and θ_b is the tilting angle of the bar that connects the endpoint of the nonlinear springs. $E_{P1}(\delta_{P1})$ represents the response of the nonlinear spring that replaces the first unit cell, $E_{P(m/2+1)}(\delta_{P(m/2+1)})$ represents the $(m/2+1)^{\text{th}}$ unit cell and $E_{Pi}(\delta_{Pi})$ represents the unit cells in between, with δ_{Pi} being the deformation of each nonlinear spring. To account for the symmetry of intermediate unit cells about the midplane (Figure 3a), the summation operator is multiplied by a factor of 2. As z_b and θ_b vary, the coordinates of the endpoints of the nonlinear springs are used to calculate first the deformation δ_{Pi} and E_{Pi} for each ring, and then E_{total}. At the deployed stable state of the snapping ring under pneumatic inflation, the ring reaches a local minimum, which can be found from the analog model by minimizing E_{total} with respect to z_b and θ_b. At the local energy minimum, the tilting angle θ_b of the rigid bar connecting the top ends of the nonlinear springs, is the analog model prediction for the bending angle of the snapping ring in its deployed stable state (further details in Section S3, Supporting Information).

To further study the role of the design variables on the bending angle at the deployed stable state, we also perform FE simulations at the ring level for bistability in bending (details in Section S1.4, Supporting Information). For demonstrative purpose, we first prescribe the beam-to-hinge thickness ratio ($t_b/t_h = 4$) to obtain the highest energy barrier, $E_{max}/E_{\min}$, for bistable snapping. This postulates two variables for a bending ring, the highest possible amplitude $(a/l)_{P1}$ of a unit cell and the gradient of amplitude $\nabla(a/l)$ as we navigate along the ring. Three rings are examined for $(a/l)_{P1}$ equal to 0.2, 0.3, and 0.4, corresponding to an increase of $\nabla(a/l)$ from 5% to 20%, 30%, and 35% respectively. For a given $(a/l)_{P1}$, an increase of $\nabla(a/l)$ results in a reduction of the smallest possible amplitude in the hexagonal ring $(a/l)_{P4}$. This sets an upper bound on $\nabla(a/l)$ in a ring to ensure that $(a/l)_{P4}$ is greater than the lower bound of 0.1 (Figure 3c).

Figure 3f reports the bending angle as a function of $\nabla(a/l)$ obtained via the structural analog, FE simulation, and experiments of a set of seven bending actuators manufactured with $(a/l)_{P1} = 0.4$ and $\nabla(a/l)$ ranging from 5% to 35% at a 5% increment. The results are in good agreement showing a linear trend of the bending angle with respect to $\nabla(a/l)$. The larger $(a/l)_{P1}$, the higher the bending angle for a $\nabla(a/l)$. Snapshots of the deployed stable state of the bending actuators are analyzed using ImageJ[58] to measure the pertinent bending angle (see Section S4, Supporting Information), and include their respective statistical dispersion in Figure 3f. The linear trend in the bending angle data obtained from a system with both material and geometric nonlinearities, is an inherent advantage of this design strategy. It eases the programming of the bending angle to ensure lockability and allows for simplified and robust predictions for varying amplitude gradients, $\nabla(a/l)$, and given amplitudes $(a/l)_{P1}$.

Similarly to the assessment of the total extensional ring of an axially stacked sequence of guiders (Section 4.1), we can here express the total bending angle θ_{total} of a multistable inflatable actuator consisting of n snapping rings as function of $(a/l)_{P1}$ and $\nabla(a/l)$ of each ring with bending angle θ_j as:

$$\theta_{\text{total}}\left((a/l)^j_{P1}(\nabla a/l)^j, n\right) = \sum_{j=1}^{n} \theta_j \left((a/l)^j_{P1},\ (\nabla a/l)^j\right) \quad (4)$$

where, $(a/l)^j_{P_i}$ and $(\nabla a/l)^j$ are the highest amplitude for a unit cell and gradient in amplitude distribution respectively in the bending ring j, θ_j is the angle at the deformed stable state for the bending ring j and n is the total number of rings in the resulting multistable guider. Both Equations (3) and (4) are key design tools for programming the response of our soft actuator as demonstrated in the following section.

5. Application of Multistable Inflatable Actuator to Soft Robotics

We now leverage the functionalities of our multistable inflatable actuator to design a soft robotic arm and a soft robotic gripper, both operating using solely a single inlet tube. The former consists of an arrangement in a series of five actuators capable to deliver motion and lockablity along programmed trajectories in extension and bending. The latter uses four actuators in parallel to grasp objects of target shape and consistency via bending multistability without continuous pressure supply. The deformation of both is reversible. Once pneumatically inflated to their deployed stable states, they can return to their initial states through pneumatic vacuum administered by a simple hand pump (Double Quick III S Hand Pump, Intex Recreation Corp, USA), hence providing electronics-free operation.

To provide context to the performance of our actuators versus existing concepts we emphasize the following. Lockability in soft robots enables operation without continuous power source, leading to energy efficiency and avoidance of puncture-induced collapse. Current pneumatic actuators in literature can primarily achieve locking in bending only.[46–51] And for non-pneumatic actuation, locking is attained in either extension[39,40] or bending;[29,31] the only non-pneumatic locking demonstrated in both deformation modes requires the continuous cooperation of two electric motors,[43] a strategy far more complex than on/off actuation. In contrast, in this work we achieve both extension and bending lockability at zero-power and with the use of a single inlet channel, thereby achieving both energy efficiency and puncture avoidance while drastically reducing the operational requirements.

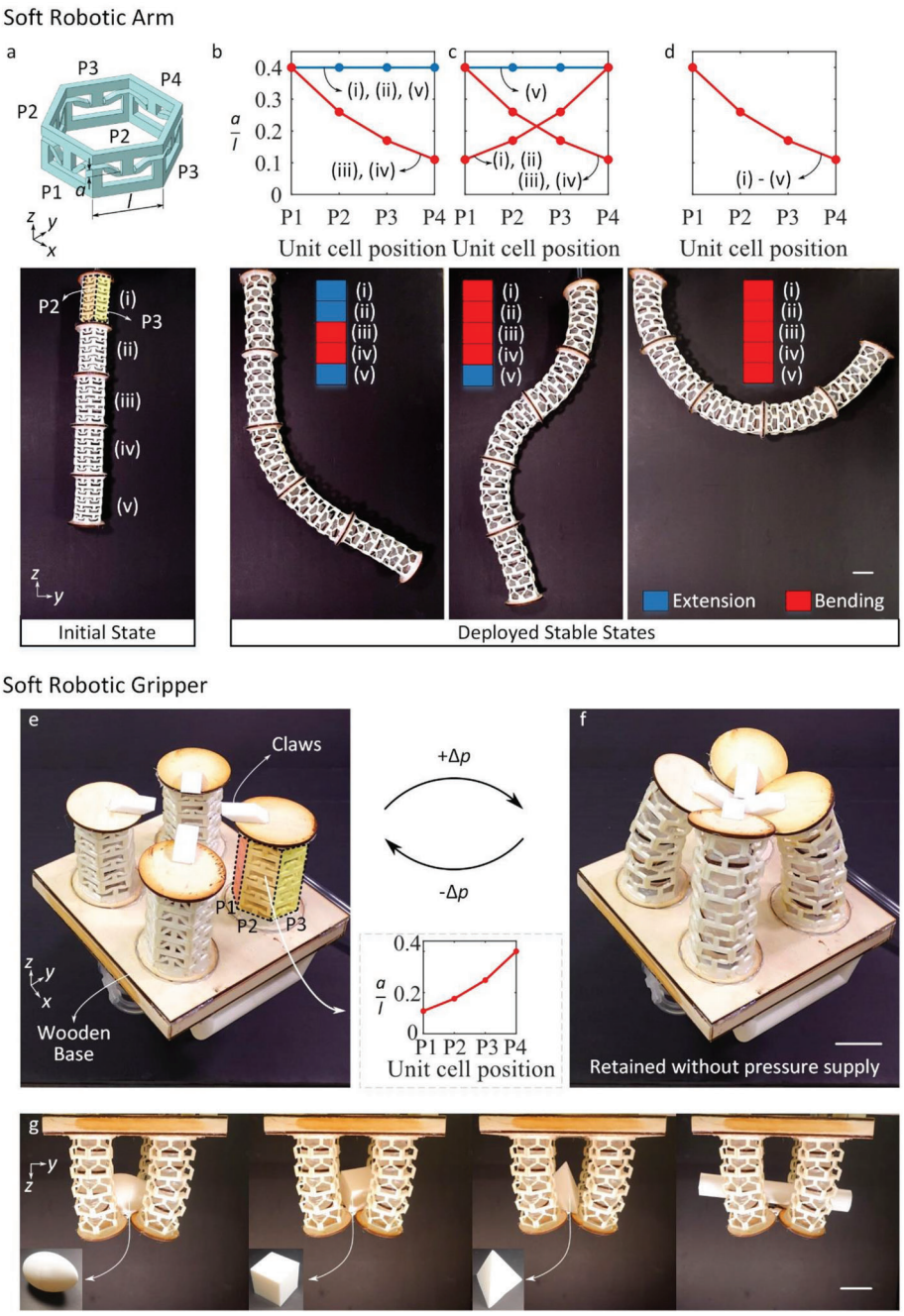

Figure 4. Soft robotic arm and soft robotic gripper retaining programmable deployed state without continuous pressure supply. a) Soft robotic arm with five segments marked (i)–(v), with all snapping rings in each segment having identical $\nabla(a/l)$. Unit cell positions, *P1–P4*, within a ring are marked (top). b–d) Multistable guider in each segment programmed to either extend or bend to attain distinct curvature values in deployed stable state under pneumatic inflation. e) Soft robotic gripper composed of four multistable bending actuators connected in parallel to a single inlet tube. f) Upon pneumatic inflation, all four actuators bend inward, resulting in a gripping action. g) Demonstration of gripper grasping and holding various fragile and irregular shaped objects at zero pressure, without causing damage to the target objects. Both arm and gripper return to the initial state under vacuum. Scale bar = 3 cm.

5.1. Pneumatic Arm

The goal here is to program the curvature of a soft robotic arm in its stable deployed state. For demonstrative purposes, we stack five multistable inflatable actuators (marked (i–v) in **Figure 4**a), each encompassing five rings and all connected to a single inlet tube. The five rings in each actuator segment are assigned with identical $\nabla(a/l)$, as per the unit cell positions marked in Figure 4a (top). By assigning either $\nabla(a/l) = 0$ or $\nabla(a/l) > 0$, each segment in the robotic arm can either extend or bend, thereby resulting in

distinct pneumatic trajectories of deployment leading to locked states that do not need continuous pressure supply. For example, the soft robotic arm in Figure 4b can attain extension and equal sign of curvature along its longitudinal axis. Segments (i), (ii), and (v), are assigned with extensional actuators whereas segments (iii) and (iv) are bending actuators with $\nabla(a/l) = 35\%$, where the unit cell with the highest amplitude in a ring occupies position *P1* and the smallest amplitude one in *P4* (graph in Figure 4b-top). This unit cell distribution enables to guide the bending deformation toward *P4* with the smallest amplitude. On the other hand, the robotic arm in Figure 4c can attain opposite curvature values. It is programmed with bending actuators in segments (i) and (ii) as well, but with unit cell positions flipped between *P1* and *P4* (graph in Figure 4c-top). The outcome of programming opposite bending in segments (iii) and (iv) is an arm with S-shaped curvature. Another example is shown in Figure 4d, where all actuators contribute to bending about one single axis. Segments (i) to (v) have identical configuration, thereby deployed in an arc that is locked in its stable state. Upon pneumatic vacuum, each of its segments returns to its initial stable state. While the significant difference in curvature obtained in these examples has been achieved by tuning only a small subset of geometric parameters, a more ample tuning capacity can be achieved by programming other geometric parameters of the actuator building blocks, as discussed in Section 4.2.

5.2. Pneumatic Gripper

The function we want to achieve in this demonstration is grasping delicate objects of various consistency and shape at zero-power. Figure 4e shows the design of our gripper comprising four identical bending actuators connected in parallel, mounted on a wooden base, and attached to a single inlet tube. Upon inflation, the robotic gripper can grasp object through claws sealed at the end plates (Figure 4e), so as to increase friction and allow for effective gripping. The multistable guider in each actuator is orientated to have the unit cells with the smallest amplitude aligned with the claws (Figure 4e). As a result, upon inflation, all four robotic fingers bend inward simultaneously, hence generating a grasping action (Figure 4f). Figure 4g demonstrates the capacity of the gripper in grabbing several objects of various shapes, sizes, and consistency, including a fragile object such as an egg (envelope dimension: 2 cm × 2.5 cm × 4 cm), which is grasped without any damage. Other shapes for the object include cubic (4 cm × 4 cm × 4 cm), tetrahedral (4 cm × 4 cm × 4 cm) as well as cylindrical (3 cm × 3 cm × 20 cm), all grasped at zero-pressure, that is, without continuous pressure input, an action enabled by the multistability of the gripping fingers. In each case, releasing the input pressure at the locked state does not impact the capacity of the gripper to hold objects of weight up to 200 g. The avoidance of a continuous pressure input to hold an object provides a robust solution for soft robots as they can become sensitive to undesired punctures and bursts. Another additional benefit is the provision of integrity to the target object especially, if fragile. A loss or reduction of pressure in a traditional pneumatic soft robot can result in the immediate fracture of the object, as opposed to our multistable actuator which can retain the object and its position even in the case of puncture or burst.

6. Conclusions

In this work, we have introduced a soft inflatable actuator with a single inlet channel that harnesses snap-through multistability to attain locking in both extension and bending. This functionality is achieved by programming the interplay between the constituents, a pneumatic transmitter *T* and a multistable guider *G*. The former takes the form of a wrinkled polyethylene cylinder with wooden ring stiffeners attached periodically onto its surface. Its function is to transfer load from the pneumatic input into *G*, which consists of a collection of tailored snapping units that guide the deformation into either locked extension or bending. Under pneumatic vacuum, *T* can restore *G* to its initial state, thereby making the actuator fully reversible. Employing either of the two alone cannot achieve these functionalities.

The concept here introduced addresses existing challenges in soft robotics. Current pneumatic actuators are unable to lock in extension, and for their non-pneumatic counterparts, locking in both extension and bending cannot be attained through a single actuation input. The advantages of enabling zero-pressure shape retention in soft robots are capitalized on two fronts, increased energy efficiency and puncture collapse avoidance. The latter is particularly important, because it reduces the probability of channel bursts associated with the prolonged pressurization needed in pneumatic robots, whereas our actuator can lock in the deployed shape with zero power, hence ensuring the safe operation of the robot in case of power shortage. We have demonstrated the effectiveness of this strategy in the design and realization of a soft robotic arm and a gripper operating through a simple hand pump and no electronics. The former can achieve programmable curvature in the deformed state, and the latter can grasp objects of various shapes and consistency up to 200 g.

Although promising, our current concept has been realized with wooden plates, which are readily available and stiff, but heavy. As a result, the self-weight of the soft robotic arm in Figure 4 limits its deformation to 2D—an issue easily mitigatable in the future by resorting to alternative materials that are stiff yet light so as to allow zero-power shape retention in 3D. Moreover, the full operation of the arm and the gripper at zero-power following inflation requires a pressure release to the atmosphere, a maneuver that for demonstrative purposes is here accomplished through the mere manual disconnect of the pressure tubing. However, for a real-life robotic application, it is necessary to integrate appropriate valves that provide independent flow control. In addition, in this work, the strategy to integrate and leverage the interplay between a pneumatic transmitter and a multistable guider has been demonstrated through one design concept. Yet there can be other design alternatives for both the transmitter and the guider, with the potential to attain additional functionalities including multiple degrees of freedom, sequential deployment, and tunable multistability.

7. Experimental Section

Materials and methods are discussed in detail in Section S1, Supporting Information, which motivates and discusses the choice of the unit cell, the fabrication process, the material characterization, and the finite element model. Section S2, Supporting Information discusses the experimental setup used to capture the pressure-volume response of the

actuator in Figure 2 and also describes the interaction between the pneumatic transmitter and the multistable guider under pneumatic vacuum. This vacuum causes the inflatable actuator to transition from its deployed stable state to its initial condensed state. An analysis of the actuator motion in the transition states is presented in Section S2.2, Supporting Information. The analog model to predict bending angle is analyzed in depth and solved for a test case in Section S3, Supporting Information, and the experimental characterization of bending angle using ImageJ is further elaborated in Section S4, Supporting Information.

Supporting Information

Supporting Information is available from the Wiley Online Library or from the author.

Acknowledgements

D.P. acknowledges the financial support of the Canada Research Chairs Program, the Natural Sciences and Engineering Research Council of Canada, and the NSERC Network for Holistic Innovation in Additive Manufacturing. S.R. acknowledges the financial support from McGill University (McGill Engineering Doctoral Award) and Fonds de recherche du Québec – Nature et technologies (FRQNT). L.W. acknowledges financial support from the China Scholarship Council (202006280037). A.E.E. acknowledges the financial support from FRQNT doctoral award. All authors thank Seung-Hyeok Han and Longyu Li for their assistance with sample fabrication.

Conflict of Interest

The authors declare no conflict of interest.

Data Availability Statement

The data that support the findings of this study are available from the corresponding author upon reasonable request.

Keywords

programmable metamaterials, snap-through multistability, soft inflatable actuators, soft robots, zero-power pneumatic gripper

Received: April 14, 2023
Revised: July 8, 2023
Published online:

[1] Y. Chi, Y. Li, Y. Zhao, Y. Hong, Y. Tang, J. Yin, *Adv. Mater.* **2022**, *34*, 2110384.
[2] Y. Cao, M. Derakhshani, Y. Fang, G. Huang, C. Cao, *Adv. Funct. Mater.* **2021**, *31*, 2106231.
[3] A. Pal, V. Restrepo, D. Goswami, R. V. Martinez, *Adv. Mater.* **2021**, *33*, 2006939.
[4] N. El-Atab, R. B. Mishra, F. Al-Modaf, L. Joharji, A. A. Alsharif, H. Alamoudi, M. Diaz, N. Qaiser, M. M. Hussain, *Adv. Intell. Syst.* **2020**, *2*, 2070102
[5] B. Gorissen, D. Reynaerts, S. Konishi, K. Yoshida, J. W. Kim, M. De Volder, *Adv. Mater.* **2017**, *29*, 1604977.
[6] B. Yu, F. Kirchner, *Soft Rob.* **2022**, 140.
[7] C. Laschi, J. Rossiter, F. Iida, M. Cianchetti, L. Margheri, *Soft Robotics: Trends, Applications and Challenges*, Springer, Berlin **2017**.
[8] A. Verl, A. Albu-Schäffer, O. Brock, A. Raatz, *Soft Robotics: Transferring Theory to Application*, Springer, Berlin **2015**.
[9] J. González-Vargas, J. Ibáñez, J. L. Contreras-Vidal, H. Van der Kooij, J. L. Pons, *Wearable Robotics: Challenges and Trends*, Springer, Cham **2016**.
[10] H. Koshima, *Mechanically Responsive Materials for Soft Robotics*, Wiley, New York **2019**.
[11] H. K. Yap, J. H. Lim, F. Nasrallah, C.-H. Yeow, *Front. Neurosci.* **2017**, *11*, 547.
[12] Y. Sun, M. Li, H. Feng, J. Guo, P. Qi, M. H. Ang Jr, C. H. Yeow, *Soft Rob.* **2020**, *7*, 30.
[13] L. Cappello, J. T. Meyer, K. C. Galloway, J. D. Peisner, R. Granberry, D. A. Wagner, S. Engelhardt, S. Paganoni, C. J. Walsh, *J. Neuroeng. Rehabil.* **2018**, *15*, 59.
[14] L. H. Blumenschein, N. S. Usevitch, B. H. Do, E. W. Hawkes, A. M. Okamura, in *2018 IEEE International Conference on Soft Robotics (RoboSoft)*, IEEE, Piscataway, NJ **2018**, pp. 245–252.
[15] E. W. Hawkes, L. H. Blumenschein, J. D. Greer, A. M. Okamura, *Sci. Rob.* **2017**, *2*, eaan3028.
[16] L. H. Blumenschein, L. T. Gan, J. A. Fan, A. M. Okamura, E. W. Hawkes, *IEEE Rob. Autom. Lett.* **2018**, *3*, 949.
[17] K. C. Galloway, K. P. Becker, B. Phillips, J. Kirby, S. Licht, D. Tchernov, R. J. Wood, D. F. Gruber, *Soft Rob.* **2016**, *3*, 23.
[18] N. R. Sinatra, C. B. Teeple, D. M. Vogt, K. K. Parker, D. F. Gruber, R. J. Wood, *Sci. Rob.* **2019**, *4*, eaax5425.
[19] F. Ilievski, A. D. Mazzeo, R. F. Shepherd, X. Chen, G. M. Whitesides, *Angew. Chem.* **2011**, *123*, 1930.
[20] Y. Li, Y. Chen, T. Ren, Y. Li, S. H. Choi, *Soft Rob.* **2018**, *5*, 567.
[21] E. Brown, N. Rodenberg, J. Amend, A. Mozeika, E. Steltz, M. R. Zakin, H. Lipson, H. M. Jaeger, *Proc. Natl. Acad. Sci. U. S. A.* **2010**, *107*, 18809.
[22] R. F. Shepherd, F. Ilievski, W. Choi, S. A. Morin, A. A. Stokes, A. D. Mazzeo, X. Chen, M. Wang, G. M. Whitesides, *Proc. Natl. Acad. Sci. U. S. A.* **2011**, *108*, 20400.
[23] A. D. Marchese, R. K. Katzschmann, D. Rus, *Soft Rob.* **2015**, *2*, 7.
[24] L. Hines, K. Petersen, G. Z. Lum, M. Sitti, *Adv. Mater.* **2017**, *29*, 1603483.
[25] J. Qi, Z. Chen, P. Jiang, W. Hu, Y. Wang, Z. Zhao, X. Cao, S. Zhang, R. Tao, Y. Li, *Adv. Sci.* **2022**, *9*, 2102662.
[26] Y.-Y. Xiao, Z.-C. Jiang, Y. Zhao, *Adv. Intell. Syst.* **2020**, *2*, 2000148.
[27] E. Yarali, M. Baniasadi, A. Zolfagharian, M. Chavoshi, F. Arefi, M. Hossain, A. Bastola, M. Ansari, A. Foyouzat, A. Dabbagh, *Appl. Mater. Today* **2022**, *26*, 101306.
[28] Y. Sun, D. Li, M. Wu, Y. Yang, J. Su, T. Wong, K. Xu, Y. Li, L. Li, X. Yu, *Microsyst. Nanoeng.* **2022**, *8*, 37.
[29] M. Follador, A. T. Conn, B. Mazzolai, J. Rossiter, *Appl. Phys. Lett.* **2014**, *105*, 141903.
[30] H. Shao, S. Wei, X. Jiang, D. P. Holmes, T. K. Ghosh, *Adv. Funct. Mater.* **2018**, *28*, 1802999.
[31] M. Follador, A. Conn, J. Rossiter, *Smart Mater. Struct.* **2015**, *24*, 065037.
[32] Q. Hu, H. Huang, E. Dong, D. Sun, *IEEE Rob. Autom. Lett.* **2021**, *6*, 1391.
[33] S.-W. Kim, J.-S. Koh, M. Cho, K.-J. Cho, *2011 IEEE International Conference on Robotics and Automation*, IEEE, Piscataway, NJ **2011**, pp. 215–220.
[34] S.-W. Kim, J.-S. Koh, J.-G. Lee, J. Ryu, M. Cho, K.- Cho, *Bioinspiration Biomimetics* **2014**, *9*, 036004.
[35] S.-W. Kim, J.-S. Koh, M. Cho, K.-J. Cho, in *2010 3rd IEEE RAS & EMBS International Conference on Biomedical Robotics and Biomechatronics*, IEEE, Piscataway, NJ **2010**, pp. 534–539.
[36] Y. Y. Xiao, Z. C. Jiang, X. Tong, Y. Zhao, *Adv. Mater.* **2019**, *31*, 1903452.

[37] J. Sun, B. Tighe, J. Zhao, in *2020 IEEE International Conference on Robotics and Automation (ICRA)*, IEEE, Piscataway, NJ **2020**, pp. 10082–10088.
[38] Z. Zhang, X. Li, X. Yu, H. Chai, Y. Li, H. Wu, S. Jiang, *Compos. Struct.* **2019**, *229*, 111422.
[39] S. Wu, Q. Ze, J. Dai, N. Udipi, G. H. Paulino, R. Zhao, *Proc. Natl. Acad. Sci. U. S. A.* **2021**, *118*, e2110023118.
[40] L. S. Novelino, Q. Ze, S. Wu, G. H. Paulino, R. Zhao, *Proc. Natl. Acad. Sci. U. S. A.* **2020**, *117*, 24096.
[41] J. A.-C. Liu, J. H. Gillen, S. R. Mishra, B. A. Evans, J. B. Tracy, *Sci. Adv.* **2019**, *5*, eaaw2897.
[42] S. J. Kim, O. Kim, M. J. Park, *Adv. Mater.* **2018**, *30*, 1706547.
[43] A. Pagano, T. Yan, B. Chien, A. Wissa, S. Tawfick, *Smart Mater. Struct.* **2017**, *26*, 094007.
[44] K. Gustafson, O. Angatkina, A. Wissa, *Smart Mater. Struct.* **2019**, *29*, 015013.
[45] P. Bhovad, J. Kaufmann, S. Li, *Extreme Mech. Lett.* **2019**, *32*, 100552.
[46] X. Ni, C. Liao, Y. Li, Z. Zhang, M. Sun, H. Chai, H. Wu, S. Jiang, *Int. J. Adv. Manuf. Technol.* **2020**, *108*, 1203.
[47] Z. Zhang, X. Ni, W. Gao, H. Shen, M. Sun, G. Guo, H. Wu, S. Jiang, *Soft Rob.* **2022**, *9*, 657.
[48] Z. Zhang, X. Ni, H. Wu, M. Sun, G. Bao, H. Wu, S. Jiang, *Soft Rob.* **2022**, *9*, 57.
[49] X. Wang, H. Zhou, H. Kang, W. Au, C. Chen, *Smart Mater. Struct.* **2021**, *30*, 125001.
[50] A. Pal, D. Goswami, R. V. Martinez, *Adv. Funct. Mater.* **2020**, *30*, 1906603.
[51] Y. Tang, Y. Chi, J. Sun, T.-H. Huang, O. H. Maghsoudi, A. Spence, J. Zhao, H. Su, J. Yin, *Sci. Adv.* **2020**, *6*, eaaz6912.
[52] J. A. Faber, J. P. Udani, K. S. Riley, A. R. Studart, A. F. Arrieta, *Adv. Sci.* **2020**, *7*, 2001955.
[53] D. Melancon, B. Gorissen, C. J. García-Mora, C. Hoberman, K. Bertoldi, *Nature* **2021**, *592*, 545.
[54] Y. Chi, Y. Tang, H. Liu, J. Yin, *Adv. Mater. Technol.* **2020**, *5*, 2000370.
[55] P. Cheng, J. Jia, Y. Ye, C. Wu, *Sensors* **2021**, *21*, 493.
[56] Y. Yang, K. Vella, D. P. Holmes, *Sci. Rob.* **2021**, *6*, eabd6426.
[57] C.-Y. Chen, K. P. May, C.-H. Yeow, in *2021 IEEE 4th International Conference on Soft Robotics (RoboSoft)*, IEEE, Piscataway, NJ **2021**, pp. 435–441.
[58] M. D. Abràmoff, P. J. Magalhães, S. J. Ram, *Biophotonics Int.* **2004**, *11*, 36.

ADVANCED FUNCTIONAL MATERIALS

Supporting Information

for *Adv. Funct. Mater.*, DOI 10.1002/adfm.202304151

Zero-Power Shape Retention in Soft Pneumatic Actuators with Extensional and Bending Multistability

*Shakurur Rahman, Lei Wu, Asma El Elmi and Damiano Pasini**

WILEY-VCH

Supporting Information

Title: Zero-power shape retention in soft pneumatic actuators with extensional and bending multistability

*Shakurur Rahman, Lei Wu, Asma El Elmi, and Damiano Pasini**

E-mail: damiano.pasini@mcgill.ca

S1. Materials and Methods

S1.1. Bistable unit cell design

Figure S1 shows the details of our unit cell geometry, which has the following prescribed dimensions for the realization of our proof-of-concept prototypes:

- horizontal span l = 22 mm,
- vertical height h =14 mm,
- hinge thickness t_h = 0.5 mm,
- hinge transition thickness t_{ht} = 1 mm,
- gap thickness t_g = 2 mm,
- vertical beam thickness t_v = 4 mm.

In addition, the snapping unit cells in Figure 1 and Figure 2 of the main text have geometric parameters of a/l = 0.4 and t_b/t_h = 4 respectively.

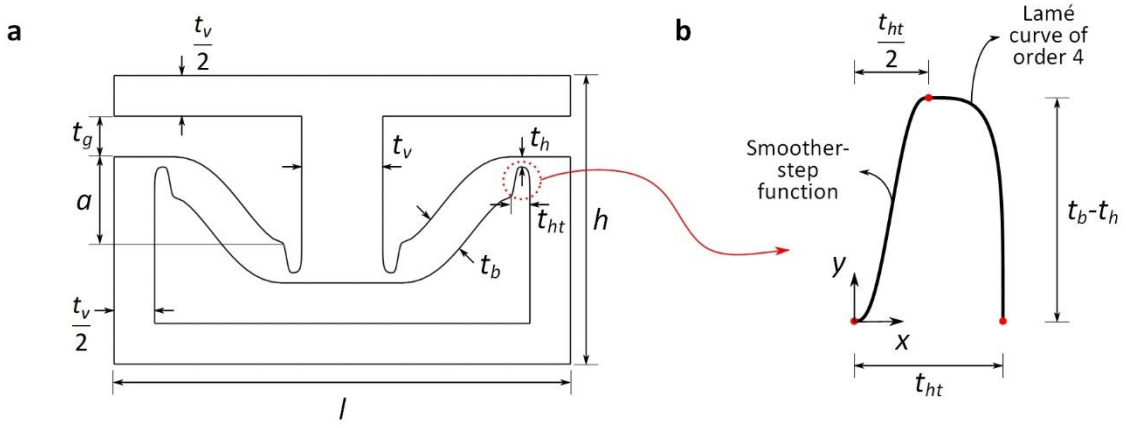

Figure S1. (a) Bistable unit cell drawing with relevant geometric parameters. (b) Hinge geometry is composed of a smoother-step function and Lame's curve of order 4.

The unit cell consists of curved beams with hinges at their point of connection with the vertical beams. The hinge profile, as shown in Figure S1b, comprises a smoother-step function[1] and a quadrant of a Lamé curve of order 4. The former provides a smooth transition for the step created due to the thick beam connected to a thin hinge. The latter completes the hinge profile,

while ensuring G2 continuity at the blending points (red). The smoother-step function for the hinge profile shown in Figure S1b is given by:

$$smootherstep(x) = (t_b - t_h)(6x^5 - 15x^4 + 10x^3), \qquad 0 \le x \le \frac{t_{ht}}{2} \tag{S1}$$

The design of the second part of the hinge profile respect the following parametric equations:

$$\left.\begin{aligned} x(t) &= \frac{t_{ht}}{2} + \frac{t_{ht}}{2} \cdot |\cos t|^{\frac{2}{n}} \\ y(t) &= \frac{t_{ht}}{2} \cdot |\sin t|^{\frac{2}{n}} \end{aligned}\right\}, \qquad 0 \le t \le \frac{\pi}{2} \tag{S2}$$

Here, *n* is the order of the Lamé curve, and is selected as 4 in this work. We select a hinged beam profile as it enhances the bistability of the unit cell as opposed to a profile without a hinge;[2] a hinged profile has the advantage of requiring higher strain energy to bring the unit cells from its deployed stable state to its closed state. The outcome is an increased robustness of the actuator, which translated into an enhanced ability to retain its deployed state without continuous pressure input, hence less vulnerable to undesired perturbations.

S1.2. Fabrication

Figure S2 shows the manufacturing of the hexagonal snapping layer, which is first segmented into six planar strips and then fabricated via fused deposition modelling (FDM) of thermoplastic polyurethane (TPU) using the Anycubic Vyper 3D printer (Shenzhen, China). The out-of-plane thickness of each strip is 2.5mm. The sides of the snapping strips are bonded with Adhaero epoxy glue (Dollarama, Canada) to create the multistable guider *G*.

Figure S3a shows the individual components of the pneumatic transmitter *T*: wooden end-plates, wooden ring-stiffeners, polyethylene cylinder and an inlet tube. The wooden components are laser cut from a flat sheet; the end plates have circular wooden stoppers attached to facilitate the bonding with the polyethylene cylinder and provide an airtight connection. Polyethylene sheet of ~0.15mm thickness are cut into the desired dimension and its sides are sealed using an impulse sealer to produce the polyethylene cylinder. The ring stiffeners are then mounted on the polyethylene cylinder. They partition the actuator in equal segments and are bonded to the

cylinder with hot-melt adhesive (Dollarama, Canada) (Figure S3b). The end-plates and the inlet tube are then attached to the assembly to complete the manufacturing of the pneumatic transmitter (Figure S3c).

Figure S2. Manufacturing of hexagonal multistable guider. (a) 3D printed planar snapping strips. (b-d) Strip bonding to realize an extruded hexagonal cross-section. Scale bar = 1cm.

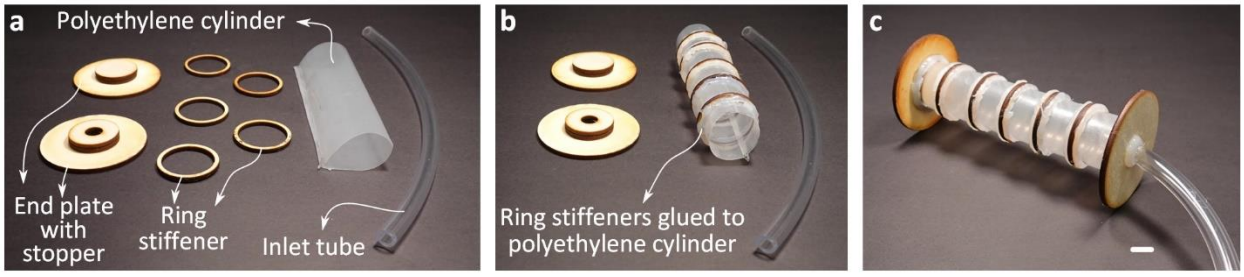

Figure S3. Fabrication of pneumatic transmitter. (a) Individual components include wooden end plates with stopper, wooden ring stiffeners, polyethylene cylinder and inlet tube. (b) Ring stiffeners are next bonded to polyethylene cylinder. (c) End plates and inlet tube are affixed in the last step. Scale bar = 1cm.

S1.3. Material Characterization

To obtain the material model of the thermoplastic polyurethane (TPU), five dog-bone-shaped specimens with dimensions as per the ASTM D638 type IV standard (**Figure S4**a) are 3D-printed using Anycubic Vyper and tested using MTS INSIGHT tensile tester (MTS Systems Corporation, Minnesota, USA). Their average nominal stress-strain response is obtained and plotted in Figure S4b.

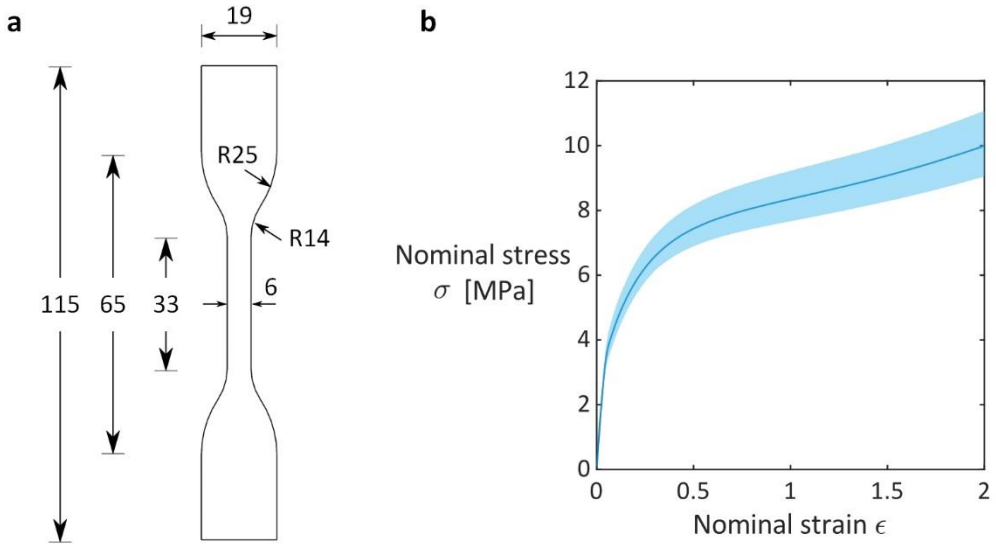

Figure S4. (a) Dimension of test samples as per ASTM D638 type IV standard, (b) Experimentally obtained nominal stress-strain response of thermoplastic polyurethane (TPU). Average data from five test specimens are plotted along with the experimental uncertainty domain.

The experimental stress-strain data is fitted through the hyperelastic Mooney-Rivlin constitutive model[3] whose strain energy potential is described by:

$$U = C_{10}(\bar{I}_1 - 3) + C_{01}(\bar{I}_2 - 3) + \frac{1}{D_1}(J-1)^2 \quad \text{(S3)}$$

Here, $\bar{I}_1 = J^{-2/3} tr\boldsymbol{B}$, $\bar{I}_2 = \frac{1}{2} J^{-4/3}[(tr\boldsymbol{B})^2 - tr(\boldsymbol{B}^2)]$ and $J = \det \boldsymbol{F}$, where $\boldsymbol{B} = \boldsymbol{F}\boldsymbol{F}^{\mathrm{T}}$ and $\boldsymbol{F}$ is the deformation gradient. Using the material constants C_{10}= -0.50695 MPa , C_{01}= 6.1538 MPa and D_1=0 MPa^{-1}, we obtain the numerical curve fitting of our experimental data.

S1.4. Finite Element Modelling

Finite element (FE) simulations are performed using ABAQUS 2021 implicit dynamic solver with quasi-static and large displacement formulations to improve convergence and account for geometric nonlinearity. All models are meshed using hybrid 8-node linear brick elements with reduced integration and hourglass control (C3D8RH). During manufacturing, each snapping strip is bonded to the sides using epoxy as mentioned in Section S1.2. This increases the axial confinement of the snapping beams as the stiffness provided by the epoxy is

considerably higher than that of TPU. To better replicate this phenomenon in our simulations, we divided the model into multiple sections, where the shaded regions in red in **Figure S5**a for the snapping ring and in Figure S5b for the unit cell, are assigned with a linear elastic material model (E=3GPa, ν=0.3) that accounts for the stiffening of the epoxy. The remaining sections are assigned with the Mooney-Rivlin material model for TPU (see Section S1.3).

For the snapping ring, the bottom is clamped and a pressure load is applied to the top surface. The loading step is divided into two sub-steps: (i) an outward pressure is applied as a ramp function, imposing the ring to undergo a maximum pressure $\Delta p = +p/p_{atm}$ and to initiate snap-through instability, and (ii) the applied pressure is linearly reduced back to zero. Following load removal, the bistability in bending is observed and the bending angle is calculated using the coordinates of the top-surface in its titled stable state.

For the unit cell, periodic boundary conditions are applied and the model is simulated under a uniaxial displacement load along *z*-axis. The strain energy data are extracted and plotted in Figure S5c and the peak energy E_{max} and local minimum E_{min} are identified. The ratio $E_{max}/E_{min} > 1$ indicates that the unit cell is bistable and its opened stable state at an energy value of E_{min} is retained following load removal.

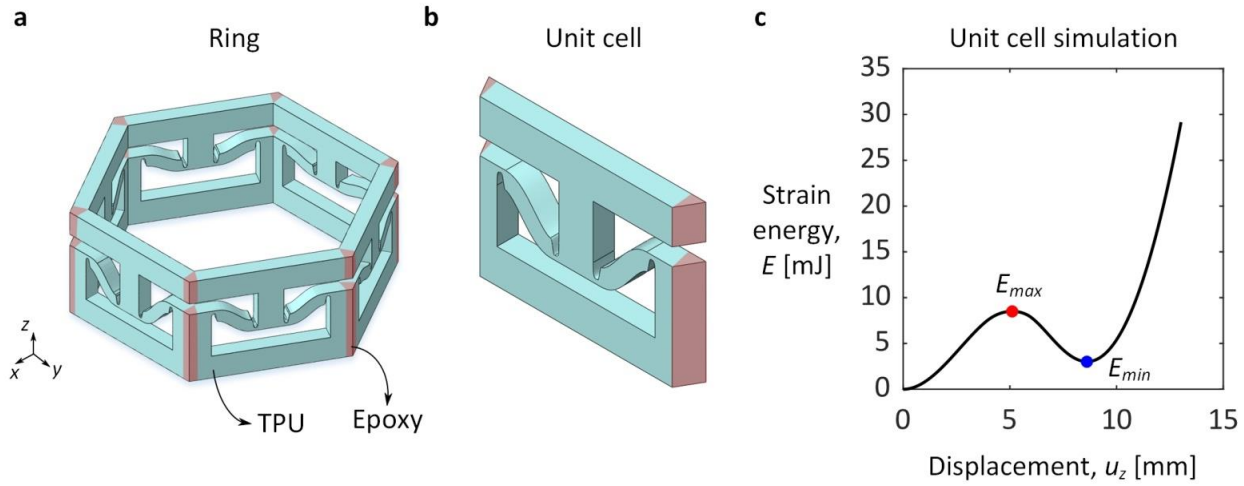

Figure S5. (a) FE model for guider ring with TPU and epoxy sections identified. (b) Unit cell FE model with epoxy on the sides. (c) Strain energy curve for unit cell deformation.

S2. Pressure-Volume Experiments for the Multistable Inflatable Actuator during Pneumatic Loading Cycle

The pressure-volume response of the multistable inflatable actuator (in Section 3 of main text) is captured using the experimental setup shown in **Figure S6**. A polypropylene syringe of 100 mL is mounted on our MTS Insight testing machine (MTS Systems Corporation, Minnesota, USA) (Figure S6a), and is connected simultaneously to the inlet tube of the actuator (Figure S6b) and a pressure sensor (HSCDRRN600MDAA3, Honeywell, USA) (Figure S6c) via a T-connector. The sensor has a maximum operating pressure of 60kPa with 1% accuracy and is controlled using an Arduino UNO microcontroller unit (Arduino, Italy). During our experiment, the crosshead of the MTS Insight machine pushes down the syringe until its full volume is dispensed at a flow rate of ~9 ml s^{-1} and then returns to its initial position, a process taking a total time of ~25 s. This completes the full inflation and vacuum cycle, during which the microcontroller reads and stores the pressure sensor data at a frequency of 20 Hz using a data acquisition software (PLX-DAQ, Parallax, USA). The experiment is repeated five times and the average response of the actuator along with the envelope that spans the test results are plotted and shown in Figure 2 of the main text and in **Figure S7** of supporting information. The former depicts the schematics and snapshots of the actuator during inflation, and the latter shows the vacuum response. In addition, we also track the actuator end plate in **Figure S8** to provide further insight into the actuator response during the intermediate steps.

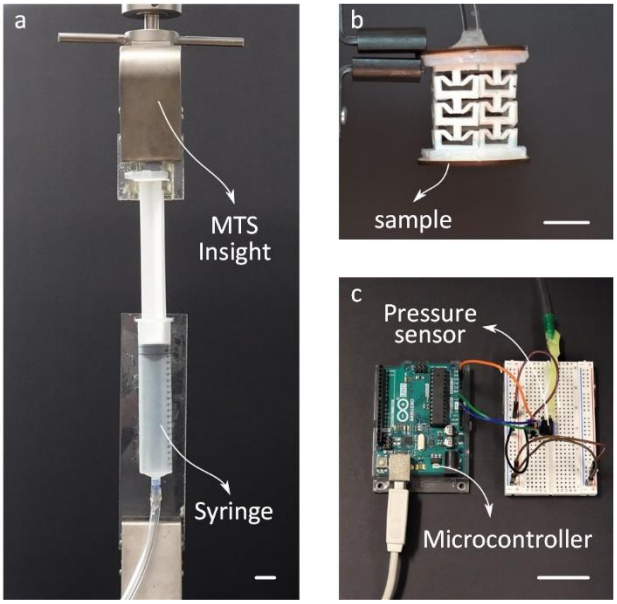

Figure S6. Experimental setup to depict pressure-volume response of the multistable inflatable actuator under pneumatic loading. Scale bar = 3cm.

S2.1. Interaction between Pneumatic Transmitter and Multistable Guider during Pneumatic Vacuum

The main text reports results for the inflation portion of the pneumatic cycle. Here we report the results for the remaining portion, the vacuum. We examine the multistable inflatable actuator in its fully extended state (Figure S7a - left) before the vacuum cycle commences (red curve in Figure S7b). Under an incremental vacuum load -Δ*p*, the polyethylene component of *T* shrinks radially, while its wooden ring stiffeners direct the end-plate deformation into axial contraction. This engages the guider, generates compression (regime II') and results in an increase in negative pressure. With further vacuuming, the negative pressure continues to increase until the energy barrier of the snapping rings is overcome, an instance that initiates sequential snap-through back to the initial, closed states. This is regime III′ of the vacuum cycle and it entails three drops in negative pressure, one per snapping ring. At the fully condensed state (regime IV′), a decrease in volume can only further compress the guider without any significant visual transformation. Figure S7c shows snapshots of the actuator at four representative points (A, B, C and D) within the three regimes of interaction under vacuum.

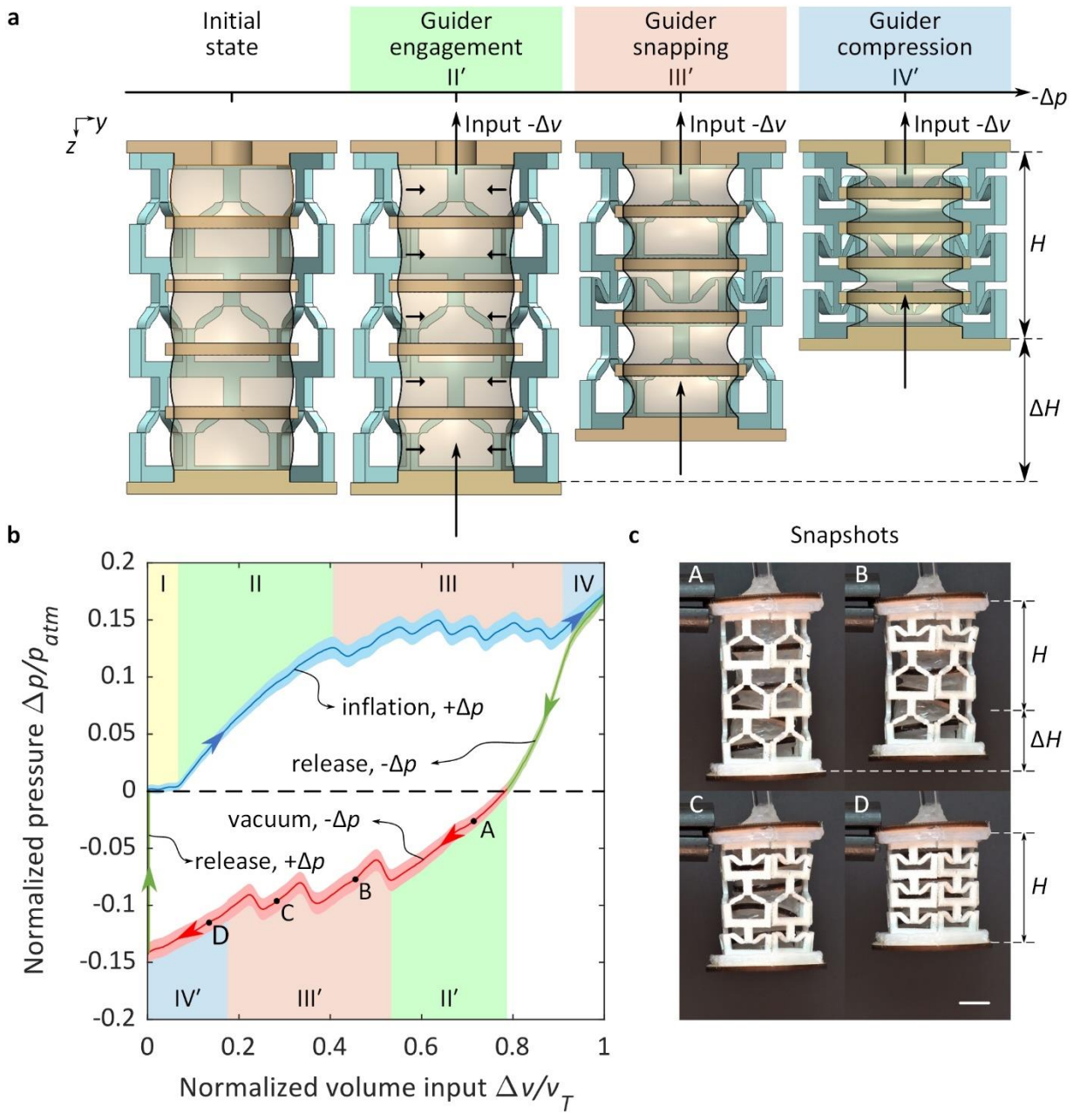

Figure S7. Interaction between multistable guider and pneumatic transmitter under pneumatic vacuum. (a) Schematics of inflatable actuator cross-section in the three regimes of interaction observed under vacuum: *guider engagement*, *guider snapping* and *guider compression*. (b) Experimental pressure-volume response of the actuator consisting of three multistable rings undergoing a pneumatic loading loop of inflation $+\Delta p$ (blue), pressure release $-\Delta p$ (green), vacuum $-\Delta p$ (red) and pressure release $+\Delta p$ (green). Regimes of interaction highlighted with pertinent colour. Uncertainty domain of experimental response indicates the dispersion of five

repetitions using one sample. Pressure normalized by atmospheric pressure p_{atm}, and volume by total volume input v_T. (c) Representative snapshots of multistable actuator under vacuum, undergoing intermediate steps of deformation from a fully deployed stable state to its initial condensed state. Scale bar = 2 cm.

S2.2. Normalized Displacement of Actuator End Plate during Pneumatic Cycle

Figure S8a shows the normalized displacement of point *P* on the actuator end plate with incremental volume during a full pneumatic loading cycle. Figure S8b depicts the snapshots of the actuator prototype at representative instances during inflation and Figure S8c during vacuum. The displacement u_z is obtained by assessing the actuator position through snapshots using ImageJ[4] and normalizing it with the height *H* of the guider. A non-linear trajectory is observed for the motion of *P* during its fully reversible deformation cycle under pneumatic loading. Although this indicates an inability to produce a smooth motion between the initial and the deployed stable states, it is, in fact, a by-product of the snapping induced bistability of the guider rings in regime III during inflation and regime III′ under vacuum. This is evident in each regime where the three jumps in the displacement values correspond to the snapping of the three rings in the actuator. While this snap-through bistability is essential to retain the deformed configuration without continuous power source, further work is required to generate a smoother motion in the transition states that undergo snap-through.

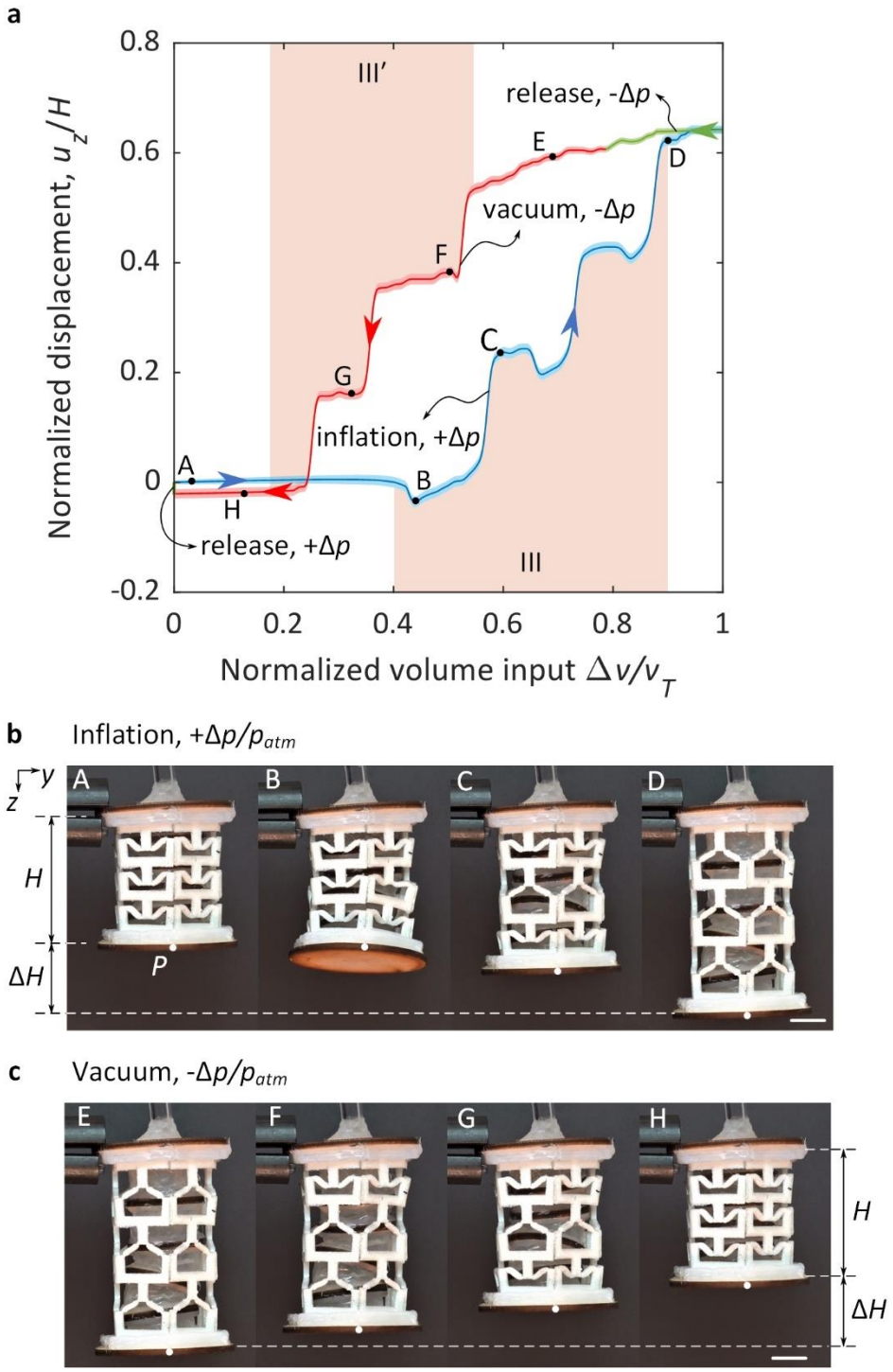

Figure S8. (a) Normalized displacement versus volume input for actuator end plate during a full pneumatic cycle of inflation +Δp (blue), pressure release -Δp (green), vacuum -Δp (red) and pressure release +Δp (green). Snapping regimes during inflation and vacuum are highlighted. The uncertainty domain of the experimental response indicates the dispersion of five repetitions

using one sample. Snapshots of actuator at representative instances during (b) inflation +Δp and (c) vacuum -Δp.

S3. Analog model

In this section, the analog model of the snapping ring presented in Section 4.2 of the main text is examined in detail. The goal is to predict the bending angle in the second stable state as the actuator is inflated. The snapping ring under investigation and its analog model are shown in **Figure S9.** They have the following characteristics: highest unit cell amplitude $(a/l)_{P1}$ of 0.4 and gradient of unit cell amplitude $\nabla(a/l)$ of 35%. The amplitude of the remaining unit cells are then calculated using Equation 1 (main text) as $(a/l)_{P2}$ = 0.26, $(a/l)_{P3}$ = 0.17 and $(a/l)_{P4}$ = 0.11. In the two dimensional (2D) analog model, nonlinear springs replace the snapping unit cells; they are clamped at their base and their top ends are connected to a rigid bar with two degrees of freedom, the vertical translation z_b and the in-plane rotation θ_b. We assume that the center of the bar does not undergo any horizontal translation in our analog model. The positions of the spring ends in their initial undeformed state, denoted by d_{Pi} for i=1, 2, 3 and 4, are representative of the positions of the unit cells with respect to the origin.

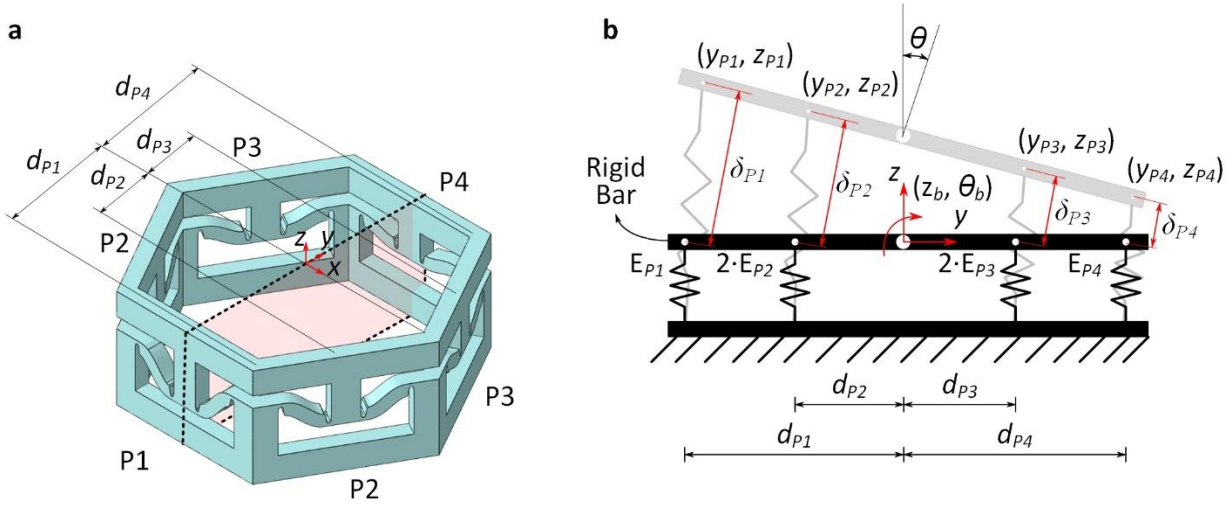

Figure S9. (a) Hexagonal snapping ring and (b) its analog model. Nonlinear elastic springs represent snapping unit cells in the analog model.

As described in Section 4.2, the total elastic energy of the analog model in Figure S9b is given by:

$$E_{total}(z_b, \theta_b) = E_{P1}(\delta_{P1}) + E_{P4}(\delta_{P4}) + 2 \cdot \left(E_{P2}(\delta_{P2}) + E_{P3}(\delta_{P3})\right) \quad \text{(S4)}$$

Here, E_{Pi} is the energy response of a nonlinear elastic spring i as a function of its deformation δ_{Pi} as i goes from 1 to 4. Their expressions are obtained via polynomial curve fitting of the strain energy data from the corresponding unit cell FE simulation as shown in **Figure S10**.

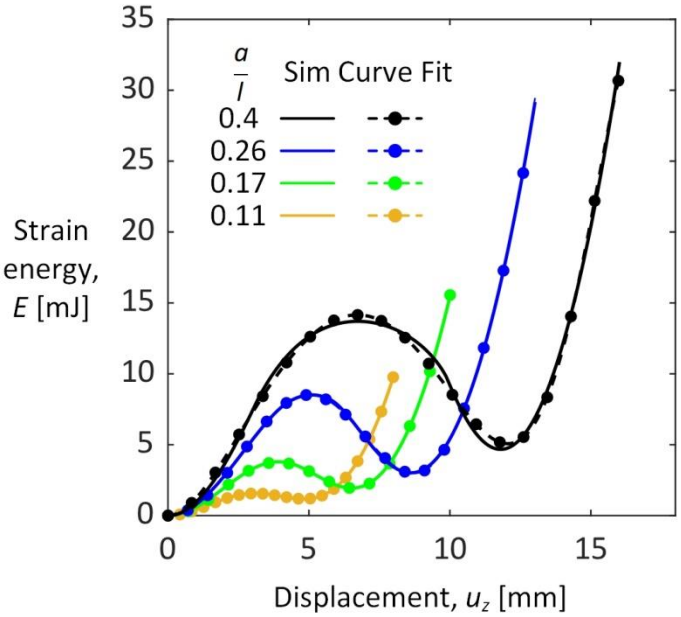

Figure S10. Polynomial curve fitting of strain energy data obtained from unit cell FE simulation for *a/l* values of 0.4, 0.26, 0.17 and 0.11 respectively.

The polynomial energy expressions for each of the springs in the analog model for this particular snapping ring are found as:

$$E_{P1}(\delta_{P1}) = -7.1986 \times 10^{-7}{\delta_{P1}}^{8} + 3.3328 \times 10^{-5}{\delta_{P1}}^{7} - 5.6323 \times 10^{-4}{\delta_{P1}}^{6} + 0.0040{\delta_{P1}}^{5} + 0.0016{\delta_{P1}}^{4} - 0.2509{\delta_{P1}}^{3} + 1.4774{\delta_{P1}}^{2} \quad \text{(S5)}$$

$$E_{P2}(\delta_{P2}) = 4.5187 \times 10^{-6}{\delta_{P2}}^{8} - 1.9488 \times 10^{-4}{\delta_{P2}}^{7} + 0.0030{\delta_{P2}}^{6} - 0.0194{\delta_{P2}}^{5} + 0.0415{\delta_{P2}}^{4} - 0.0906{\delta_{P2}}^{3} + 0.8198{\delta_{P2}}^{2} \quad \text{(S6)}$$

$$E_{P3}(\delta_{P3}) = 9.8354 \times 10^{-6}{\delta_{P3}}^{8} - 3.1370 \times 10^{-4}{\delta_{P3}}^{7} + 0.0034{\delta_{P3}}^{6} - 0.0123{\delta_{P3}}^{5} - 0.0055{\delta_{P3}}^{4} - 0.0266{\delta_{P3}}^{3} + 0.6210{\delta_{P3}}^{2} \quad \text{(S7)}$$

$$E_{P4}(\delta_{P4}) = 1.0935 \times 10^{-5}{\delta_{P4}}^{8} - 2.3802 \times 10^{-4}{\delta_{P4}}^{7} + 0.0012{\delta_{P4}}^{6} + 0.0059{\delta_{P4}}^{5} - 0.0507{\delta_{P4}}^{4} - 0.0139{\delta_{P4}}^{3} + 0.4641{\delta_{P4}}^{2} \quad \text{(S8)}$$

Here, the deformation δ_{Pi} for spring i =1, 2, 3 and 4 are calculated as:

$$\delta_{Pi} = \sqrt{\left(y_{Pi} - y_{Pi}^{0}\right)^{2} + \left(z_{Pi} - z_{Pi}^{0}\right)^{2}} \quad \text{(S9)}$$

where, y_{Pi}^{0} and z_{Pi}^{0} are the coordinates of the springs ends in their initial undeformed state, y_{Pi} and z_{Pi} are the coordinates in their deformed state and can be calculated as $y_{Pi} = y_{Pi}^{0}\cos\theta_{p}$ and $z_{Pi} = z_{b} + y_{Pi}^{0}\sin\theta_{p}$. As the connecting bar undergoes rigid body translation z_b and rotation θ_b about its center, the second stable state of the analog model can be found by minimizing the energy expression in Equation S4. With z_b and θ_b as design variables, the optimization problem can be formulated as:

$$\min_{z_b,\theta_b} E_{total}(z_b,\theta_b) \quad Subject\ to \begin{cases} z_b > 0 \\ \theta_b > 0 \\ z_{Pi} > 0, & i = 1,2,3,4 \\ \delta_{Pi} > \delta_{Pi}^{E_{max}}, & i = 1,2,3,4 \end{cases} \quad \text{(S10)}$$

The inequality constraints in the optimization framework are imposed to guide the convergence of the design variables to a practical solution. In its deformed stable state, the snapping ring will undergo positive vertical translation and tilt about the unit cell with the

smallest amplitude. Imposing $z_b > 0$ and $\theta_b > 0$ ensure these practical considerations are accounted for in our formulation. In addition, the unit cells only experience tensile loading as they are inflated, and the inequality constraint $z_{Pi} > 0$ for each unit cell *Pi* prevents from applying any compressive force. Finally, $\delta_{Pi}^{E_{max}}$ is the deformation of unit cell *Pi* in its peak strain energy E_{max}, and the constraint $\delta_{Pi} > \delta_{Pi}^{E_{max}}$ ensures that all unit cells in the converged solution are in the deployed state.

In this study, the nonlinear constrained optimization problem in Equation S10 is implemented and solved in MATLAB (MathWorks, Massachusetts, USA) using the built-in 'fmincon' function, which iteratively updates the design variables via the Broyden-Fletcher-Goldfarb-Shanno (BFGS) method[5] until convergence is reached. For the snapping ring in Figure S9, the converged solution is (z_b, θ_b) = (4.6027, 8.9007), which is a local minimum for the total strain energy E_{total} of the system as can be seen from the contour plot in **Figure S11**. The angle θ_b is the analog model prediction for the bending angle of the snapping ring with $(a/l)_{P1}$ = 0.4 and ∇(a/l) = 35% in its second stable state under pneumatic inflation.

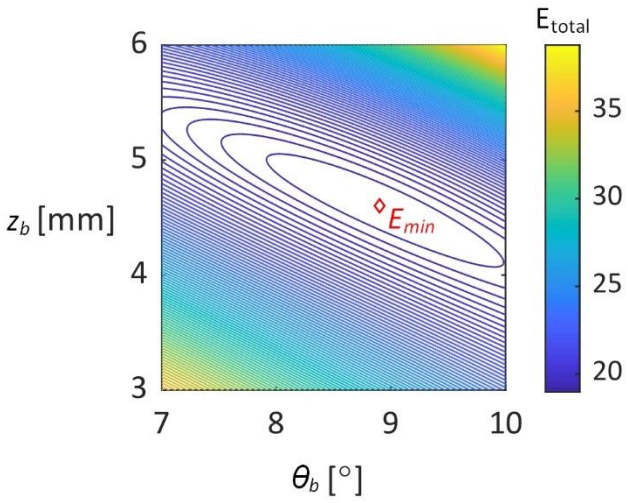

Figure S11. A contour plot for the total strain energy of deformation obtained from the analog model of a snapping ring with $(a/l)_{P1}$ = 0.4 and ∇(a/l) = 35%. Red diamond represents converged point of the optimization problem.

In this work, we solve a set of analog models for snapping rings with $(a/l)_{P1}$ of 0.2, 0.3 and 0.4 as ∇a/l increases from 5% to 20%, 30% and 35% respectively. The results are plotted in

Figure 3e (main text) and show a good agreement with the results from our FE simulations and experiments.

S4. Experimental Characterization of Bending Angle

To validate the bending angle obtained using FE simulations and our analog model, seven inflatable actuators are manufactured with the highest unit cell amplitude $(a/l)_{P1}$ of 0.4 as the gradient of amplitude $\nabla(a/l)$ increases from 5% to 35% in increments of 5%. Each actuator has five identical snapping rings. They are clamped vertically and inflated until all the rings snap to their second stable state. The pressure source is then removed and a photograph of the actuator in its deformed state is captured as shown in **Figure S12**, and analyzed using ImageJ.[4] The tilting angle θ of the actuator end-plate provides the bending angle produced by five identical rings, from which the bending angle per ring is calculated. The experiment is repeated five times for each actuator; the mean bending angle and standard deviation are calculated and plotted in Figure 3 (main text). The latter constitutes the error bar in the plot.

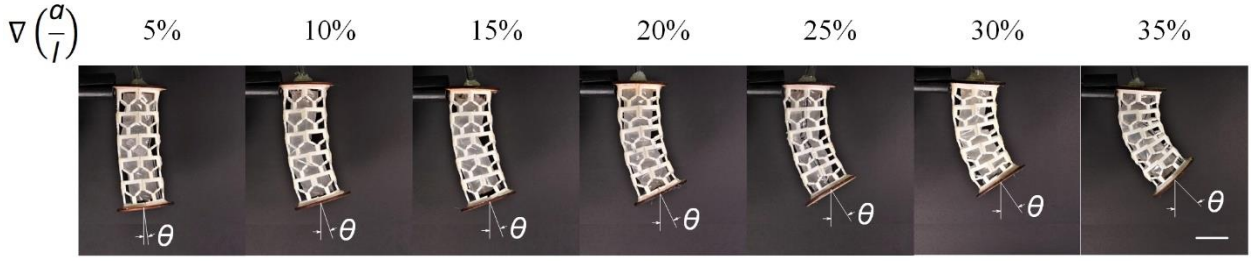

Figure S12. Snapshots of seven bending inflatable actuator with increasing $\nabla(a/l)$ in their deformed stable state. The experiment is repeated five times for each actuator. Scale bar = 3cm.

References

[1] D. S. Ebert, F. K. Musgrave, D. Peachey, K. Perlin and S. Worley, *Texturing & modeling: a procedural approach*. Morgan Kaufmann, 2003.

[2] J. Qiu, J. H. Lang and A. H. Slocum, "A curved-beam bistable mechanism," *Journal of microelectromechanical systems,* vol. 13, no. 2, pp. 137-146, 2004.

[3] Z. Meng, M. Liu, H. Yan, G. M. Genin and C. Q. Chen, "Deployable mechanical metamaterials with multistep programmable transformation," *Science Advances,* vol. 8, no. 23, p. eabn5460, 2022.

[4] M. D. Abràmoff, P. J. Magalhães and S. J. Ram, "Image processing with ImageJ," *Biophotonics international,* vol. 11, no. 7, pp. 36-42, 2004.
[5] P. E. Gill, W. Murray and M. H. Wright, *Practical optimization*. SIAM, 2019.